Journal of Power Sources 670 (2026) 239535

Contents lists available at ScienceDirect

Journal of Power Sources

journal homepage: www.elsevier.com/locate/jpowsour

Quantification of [MTBD][beti] loading and its effects on Pt/HSC electrode performance in hydrogen fuel cells

Marc Manyé Ibáñez [a,b], Adam Holewinski [a], J. Will Medlin [a], Tim Van Cleve [b,*], K.C. Neyerlin [b,**]

[a] University of Colorado, Boulder, CO, 80309, USA
[b] National Renewable Energy Laboratory, Golden, CO, 80401, USA

HIGHLIGHTS

- Sequential deposition improves IL deposition efficiency and pore filling.
- Up to 28% boost in mass activity with minimal IL loading.
- E*x situ* and *in operando* characterization to describe local distribution of IL within electrode.
- ILs reduce sulfonate adsorption on Pt sites and enhance ionic conductivity at low RH.
- Excess IL worsens gas transport causing non-monotonic performance trend with IL loading.

GRAPHICAL ABSTRACT

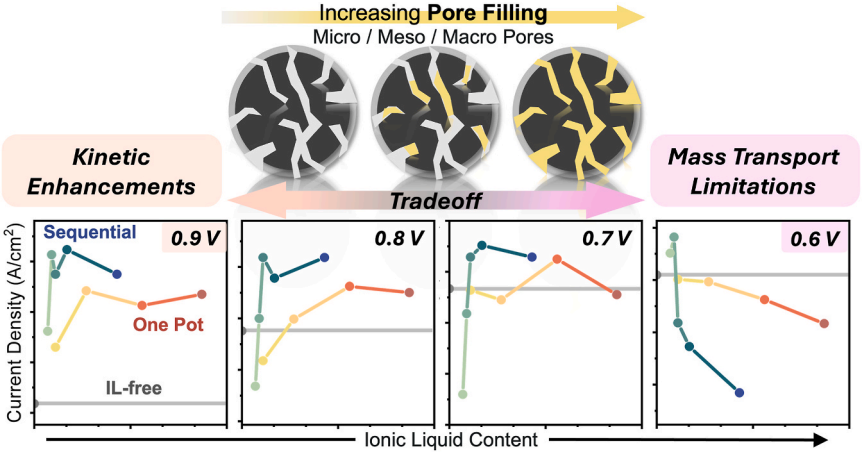

ARTICLE INFO

Keywords:
Proton exchange membrane fuel cells (PEMFC)
Ionic liquids
Selective pore filling
Modification of electrochemical interfaces
Component integration into electrodes

ABSTRACT

High surface area carbon-supported platinum catalysts (Pt/HSC) are widely used in polymer electrolyte membrane fuel cells but often suffer from limited proton and oxygen transport within porous domains. To address these challenges, we integrate the ionic liquid [MTBD][beti] into Pt/HSC catalyst layers using two deposition methods—one-pot and sequential deposition—to tune IL distribution within micropores and mesopores. A combination of *ex situ* and *in operando* techniques were employed to elucidate electrode structure–performance relationships across a range of IL loadings. Sequential deposition achieved more efficient pore filling and higher IL retention at lower IL:C ratios, enabling enhanced proton conductivity and protection of active sites. Compared to the IL-free Pt/HSC, IL-modified electrodes demonstrated up to 28% improvement in mass activity and enhanced high-current-density performance under low relative humidity, while maintaining comparable performance under humidified conditions. Electrochemical impedance spectroscopy and CO displacement

* Corresponding author.
** Corresponding author.
E-mail addresses: timothy.vancleve@nlr.gov (T. Van Cleve), kenneth.neyerlin@nlr.gov (K.C. Neyerlin).

https://doi.org/10.1016/j.jpowsour.2026.239535
Received 31 October 2025; Received in revised form 21 January 2026; Accepted 1 February 2026
Available online 7 February 2026

experiments reveal that improvements are linked to reduced ionic resistance and lower sulfonate adsorption on Pt sites, rather than changes in electrochemical surface area. However, excessive IL loading leads to mass transport losses. These results highlight the importance of selective pore filling and efficient IL distribution in achieving kinetic gains without compromising ionic and gas transport.

1. Introduction

Polymer electrolyte membrane fuel cells (PEMFCs) stand out among electrochemical energy conversion technologies as a promising solution to heavy duty transport, stationary power and remote applications [1,2]. PEMFCs are renowned for their high energy efficiency, energy density, load following, and responsiveness [3,4]. However, the commercialization of PEMFCs remains hindered by the high material cost of platinum (Pt) catalysts, driving the need for more active, durable, and cost-effective electrodes with reduced Pt loadings. A key limitation is the sluggish cathode oxygen reduction reaction (ORR) kinetics, which results in significant overpotentials and limits power density, necessitating higher loadings of the scarce and expensive Pt electrocatalyst [5,6]. The U.S. Department of Energy (DOE) has established a target to reduce the cost of PEMFC systems to below $60/kW by 2030, with a peak efficiency of 72% and 30,000 h of durability [7]. These goals have accelerated efforts to develop more active and durable electrocatalysts with a premium on high current density performance, as end of life power density dictates minimum stack size. Furthermore, high current-density (HCD) performance is often constrained in low-Pt electrodes by limited gas transport through ionomer films and/or liquid water, which also act as ionic transport pathways to active sites, complicating electrode design [8–11].

Fuel cell electrodes consist of Pt catalyst nanoparticles supported on porous carbon particles, with an ionically conductive polymer (ionomer) deposited over the carbon surface. Commonly used carbon supports include graphitized solid carbons, such as Vulcan, and high-surface-area porous carbons (HSC), like Ketjen Black. The structure, morphology of the carbon support, and location of the metal catalyst particles play a crucial role in determining fuel cell performance and durability. On solid carbon supports, Pt catalyst particles are generally exposed to the ionomer, leading to ionomer adsorption on the Pt surface. This interaction can reduce the ORR activity, often by a factor of 2–4, as well as limit O_2 transport at high current densities [12,13]. In contrast, on HSCs, a significant fraction of Pt catalyst particles reside within the carbon porous structure. When the pore openings are smaller than the hydrodynamic size of the ionomer (typically 2–7 nm), these internal catalyst sites can be shielded from the ionomer, (i) limiting proton access to the active sites at low relative humidity (RH), and (ii) decreasing interactions with the ionomer network exhibiting high kinetic activities. At high RH, this is not an issue since water can access the active sites inside smaller pores and provide enough conductivity [14]. However, at low RH, HSCs are often hindered by increased mass transport losses due to the limited proton and oxygen transport within the mesopores [15], where Pt sites can become inactive due to poor ionomer penetration and reduced ionic conductivity pathways. Consequently, the restricted accessibility to Pt sites in the porous carbon structure also increases oxygen transport resistance, impeding overall fuel cell performance [16–18].

In this work, we integrate ionically conductive, high-oxygen-solubility ionic liquids (IL) into PEMFC catalyst layers with a commercial Pt/HSC catalyst as a strategy to enhance their performance. The ILs are anticipated to penetrate the micro-, meso-, and macropores of the support to improve ionic and reactant accessibility of the pore-confined catalyst particles, and enhance homogeneity of the ionic network, addressing discontinuities in the ionomer phase that lead to lower site activity at low RH. By enhancing ionomer connectivity, ILs can reduce the dependence on external RH conditions and mitigate transport losses within porous HSC supports. In particular, the micro- and macropore domains critically influence local and bulk proton and oxygen transport, respectively, within the cathode catalyst layer, impacting high-current-density performance [19]. Prior studies have shown that micropore openings on the carbon particle surface can impose significant oxygen transport resistance, as oxygen must diffuse through these narrow channels to reach Pt nanoparticles in mesoporous regions [17,18]. Simultaneously, the macropore volume strongly correlates with the distribution of ionomer, where excessive macropore volume can disrupt the uniformity of the ionomer film, leading to increased proton transport resistance through the electrode layer due to greater ionic tortuosity [18].

The addition of ILs such as [MTBD][beti] has been explored in rotating disc electrode (RDE) setups and has been shown to substantially boost ORR performance by improving the kinetics and ionic conductivity in an aqueous environment [20–26]. Despite promising early work in RDE experiments, the practical implementation of ILs in membrane electrode assemblies (MEAs) has encountered challenges, including controlling local IL distribution and retaining IL within the electrode structure during testing. ILs can modulate hydrophilic and hydrophobic interactions within the catalyst layer, influencing the conformational behavior of Nafion chains near Pt surfaces and within the porous structure. Hydrophobic ILs with minimal water uptake are particularly advantageous, as they reduce electrostatic repulsion on Nafion chains while preserving water layers near the Pt surface that facilitate proton conductivity [27]. Because of that, it is hypothesized that the addition of the [MTBD][beti] IL could protect the Pt surface from SO_3^- poisoning. However, too much IL could hinder O_2 transport, analogous to issues with excess ionomer within catalyst layers, as O_2 permeability within the IL phase is lower than in empty pores.

This expectation aligns with the findings of an earlier study of ILs in scale-up MEAs, which proposed that the optimum IL loading has less than 30% of the IL located on the external surface or bigger pores, and about 70% of the IL is deposited in the micro- and smaller mesopores [27]. This distribution enables the IL to remain confined within smaller pores, where it facilitates proton transport through support-IL interactions while mitigating rapid IL dissolution [27]. These results demonstrate the importance of selectively filling specific pore domains to enhance catalyst layer functionality and stability under operational conditions.

While the performance benefits of ILs in RDE systems have been widely studied, their application in scaled-up MEAs remains less understood. In the developed methodology, we aim to address these challenges by preferentially filling of the micropores to mitigate oxygen transport resistance and improve mass activity, while partially filling mesopores and macropores to enhance connectivity within the ionomer network, ensuring improved catalyst layer performance under varying operational conditions. This approach involves varying nominal IL loadings to achieve different pore fillings using two different synthesis methods to evaluate IL impregnation efficiency, its correlation to pore penetration, and its impact on electrode performance on fully conditioned fuel cell MEAs at beginning of life. *In operando* electrochemical characterization of electrodes will be used to further elucidate changes in ionic conductivity, Pt site accessibility, and the sulfonate coverage on active Pt sites within IL-modified electrodes relative to IL-free Pt/HSC electrodes.

2. Results and discussion

2.1. Synthesis of IL-modified samples

Protic [MTBD][beti] ILs have been used in literature for similar applications due to their unique properties that align with design principles of impregnating catalyst layer pores with a secondary phase of high oxygen solubility. This hydrophobic IL can enhance oxygen retention within ~2 nm pores near catalytic surfaces, promoting frequent interactions while expelling water via capillary forces. Its protic nature facilitates proton transfer to the catalytic surface for the ORR, and its thermal stability ensures durability under operating conditions [20]. Among the superbase-derived ILs developed by Luo et al. [28], [MTBD][beti] offers a good balance of hydrophobicity, thermal stability, and high oxygen solubility relative to water, making it an ideal candidate for this application.

Fig. 1A presents a schematic representation of HSC pores, highlighting our aim to control pore filling within different pore sizes to achieve performance differences. To investigate the effectiveness of IL pore impregnation, two synthesis methods were used. In the one-pot deposition (OP) method, the IL is synthesized *ex situ* through a proton transfer reaction by mixing the solution of the cation $[MTBD]^+$ with the precursor containing the anion $[beti]^-$. The resulting IL is then added to the previously wetted catalyst powder and then sonicated to facilitate IL distribution and penetration into the pores of the catalyst. In the sequential deposition (SD) method, the cation and anion are added sequentially to synthesize the IL in the catalyst pore domains. The cation $[MTBD]^+$ solution is first mixed with the catalyst and slowly evaporated to let the cation impregnate the pores. Then, the dry cation-loaded catalyst is collected and transferred to a solution with the anion component, so the IL synthesis reaction is hypothesized to happen inside the pores.

In the developed methodology, we aimed to provide a range of pore fillings, from partially filled micropores to fully filled micropores and mesopores, to capture the wide range of IL loadings proposed in literature, and measure their impact on performance and electrode properties, which were later correlated with IL loading for both one-pot and sequential deposition methods. To align with the target IL pore fillings, we calculate the nominal IL:C ratios and use these ratios consistently in the sample labels referring to specific samples throughout the manuscript, acknowledging that the actual IL loadings may vary based on the characterization of pore volume and IL mass by BET and TGA, respectively. It is important to note that the IL-free sample is labeled as IL:C ratio of 0, even though all the samples were fabricated with a constant ionomer (D2020) to carbon mass ratio of 0.6.

2.2. Characterization of IL-modified samples

Catalyst powders were characterized using N_2 physisorption measurements followed by analysis of the surface area and pore size distribution using the Brunauer–Emmett–Teller (BET), Barrett-Joyner-Halenda (BJH) methodologies, and t-plot analysis. Fig. S1 shows N_2 isotherms that represent the adsorption/desorption profile of the HSC and IL-modified catalysts with a characteristic Type IV isotherm shape (IUPAC classification) [29]. A sharp rise in N_2 uptake is observed at ~0.5 relative pressure, indicating the presence of ordered mesoporosity, while another steep rise under lower partial pressures is a characteristic of systems containing micropores. Based on IUPAC definitions, we define these pore regimes by diameter: micropores (<2 nm), mesopores (2–50 nm), and macropores (>50 nm) [29]. Nevertheless, deconvoluting the carbon pore structure according to these strict definitions is challenging in HSCs. Fig. S2 shows BJH pore volume distributions, where for all the catalysts, we can see a sharp rise in N_2 adsorption volume at ~4 nm, reflecting mesoporous contributions, followed by a plateau near ~8 nm and an additional increase at higher diameters indicative of macroporosity. Due to the narrow distribution of pore sizes of these materials, pores are classified as micropores (<2 nm), mesopores (2–8 nm), and macropores (>8 nm). These definitions ensure that we can capture the main regions of interest relevant to high surface area carbons commonly used as fuel cell catalyst supports and follow a previously suggested classification [18,30].

The IL-free catalyst has a total BET surface area of 486.2 $m^2/g_{catalyst}$, which is expected for a Pt/HSC and decreases with the amount of IL added in the modified samples. Table S1 summarizes the total surface area and contributions from various pore sizes. Fig. S3A illustrates that the surface areas for the different pore regions show similar surface area blocking trends consistent with the pore filling with increasing IL loading. Fig. 1B shows BET pore volume and micro + meso pore filling as a function of the nominal IL:C ratio for the IL-free Pt/HSC and IL-modified samples. Pore filling is calculated by subtracting the pore volume of the IL-samples from BET with the pore volume of the IL-free sample.

Comparing the different synthesis methods in Fig. 1B, we can see that one-pot IL-samples require higher IL loadings to achieve a similar pore filling compared to the sequential deposition. The one-pot synthesis also appears to fill micropores and mesopores equally. The filling distribution can be observed when comparing the OP 0.11 and OP 0.27 IL:C samples. As nearly half of the micropores are filled, the mesopores are also filled to a similar extent. Consequently, it is challenging to selectively fill micropores with this method, as they are not fully filled even at higher IL:C ratios. In contrast, sequential deposition samples appear to

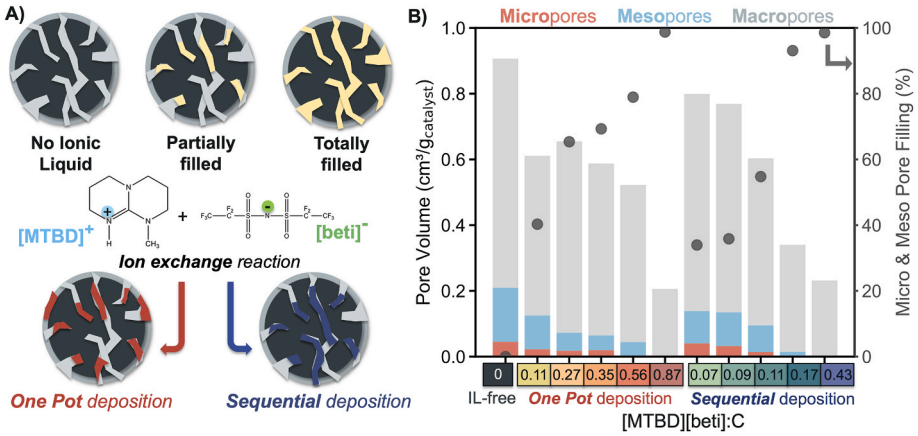

Fig. 1. A) Schematic representation of HSC pores, IL pore filling, and [MTBD][beti] synthesis methodologies. B) BET pore volume as a function of the nominal IL:C ratio for the two different syntheses. Micropores (<2 nm) in red, mesopores (2–8 nm) in blue, and macropores (>8 nm) in grey; micro and meso pore filling on the secondary y axis with circles. (For interpretation of the references to color in this figure legend, the reader is referred to the Web version of this article.)

selectively fill micropores even at low IL:C ratios. We observe higher penetration into these pores and a more selective deposition. Comparing SD 0.09 and SD 0.11 IL:C samples, mesopores do not begin to get filled until almost all micro pores are filled. To confirm the reproducibility of the N_2 physisorption measurements, Fig. S4 presents data from triplicate analyses of both the IL-free sample and the SD 0.07 IL-modified sample, demonstrating consistent results across measurements.

To visualize the differences in pore filling at the same nominal IL:C scale, Fig. 2 shows pore filling for the total pores (A), micropores (B), mesopores (C), and macropores (D) as a function of the IL:C ratio for the two different synthesis methods. A more consistent and rapid increase in pore filling at lower IL:C ratios is observed for the sequential deposition method. Less than 0.2 IL:C is required to fill all micropores and nearly all mesopores. Overall, the sequential deposition shows higher slopes compared to the one-pot, indicating better control over the deposition process when filling micropores and mesopores. Interestingly, Fig. S9 shows pore fillings across both one pot and sequential deposition methods converge when normalized by actual IL:C ratio measured from TGA.

To further examine the amount of IL deposited relative to the volume quantified by N_2 physisorption, thermogravimetric analysis (TGA) was conducted on the IL-free and IL-modified samples. After drying pre-treatment, all weight loss in the Pt/HSC catalyst is attributed to carbon oxidation, with the remaining weight representing the Pt content of the catalyst [31]. For IL-modified samples, the IL wt% is determined by subtracting the remaining wt% of the sample from the IL-free Pt wt%. Since IL increases the overall mass of the sample, the remaining wt% in the IL samples is lower than that of the IL-free catalyst. Fig. S5 shows replicate TGA experiments for the IL-free catalyst, showing an average of 53.15 ± 0.01 Pt wt% content in the sample, which is slightly higher than the expected 47.7 wt% provided by the catalyst manufacturer.

Fig. S6 shows the TGA control experiment of just [MTBD][beti], compared with the IL-free baseline, which demonstrates the stability of the additive until 400 °C, which makes this additive appropriate even for high-temperature heavy-duty applications. This result also aligns with the temperature stability of other protic ionic liquid studies, where they are exposed to high temperatures [28]. Fig. S7 presents the TGA results for all the OP samples, highlighting decreasing consistency at higher IL loadings. Notably, the OP 0.56 sample retained 7.29 wt% at the end of the measurement, indicating a significantly higher IL content than expected. In contrast, OP 0.87, which is expected to contain more IL, showed 31.79 wt%, suggesting high sample heterogeneity especially for high IL loading catalyst. The clear outlier behavior of OP 0.56, along with the observed lower IL retention at higher nominal IL:C ratios, points to challenges in achieving efficient IL impregnation and uniform penetration within the pores using the OP method. In contrast, TGA for SD IL-modified samples shown in Fig. S8 presents a more consistent trend across the loadings compared to the nominal loading used during the synthesis.

Fig. 3A shows a parity plot comparing the actual mass of IL from TGA with the nominal mass of IL. Clear differences are observed between the synthesis methods, with sequential deposition showing a slope close to 1, indicating a high uptake efficiency compared to the one-pot, which has a lower slope of 0.61. This implies that the OP method only deposits ~61% of the IL starting material, meaning higher nominal IL loadings are needed to achieve identical mass and volume loadings as SD-deposited IL electrodes, which were roughly 96% effective. Any decrease in slope is assumed to be a function of synthesis efficiency, which is hypothesized to be partially correlated to IL retention during synthesis, further discussed in the supporting information.

Fig. 3B shows the mass of IL determined from TGA compared to the inaccessible volume measured from BET. The inaccessible pore volume, which is effectively the IL volume and any blocked volume, is calculated by subtracting the total pore volume of the IL-free sample (0 IL:C) from the total pore volume of the IL-modified samples. Both synthesis methods are in agreement, showing increasing TGA IL mass loading well-correlated with increasing inaccessible volume from N_2 physisorption; however, the data reveal lower IL masses than expected from the apparent pore filling based on these measurements. Since both quantities are normalized by total catalyst mass (inclusive of IL), the slope should be a straight line with a constant value equivalent to the IL density. [MTBD][beti] has a density ~1.5 g/cm^3 [30], represented with the green line in Fig. 3B. All the data points from OP and SD samples lie along a grey line corresponding to an effective density of 0.29 ± 0.03 g/cm^3 calculated from a linear regression. This observation suggests that IL deposition leads to significantly higher (~5x) pore filling or blocking than would be expected from the IL alone (based on mass loading from TGA). It is unclear how IL depositions within porous carbons might affect N_2 physisorption and if these volumes are inaccessible under relevant fuel cell operating conditions.

2.3. MEA characterization

Fuel cell performance and electrochemical characterization of IL-modified Pt/HSC electrodes were evaluated in 50 cm^2 catalyst-coated membranes (CCMs) following established M2FCT testing protocols [32]. MEA performance improved after several voltage recovery (VR) cycles, with peak performance stabilizing after the third cycle, as shown in Figs. S11 and S12. While additional recovery cycles can further boost performance, the first VR cycle appears to remove the majority of contaminants and impurities that were introduced during the fabrication, assembly, or initial warm-up, since the minimal performance gains are observed after this step. As prepared, IL-modified electrodes show worse initial performance before conditioning, but the conditioning protocol

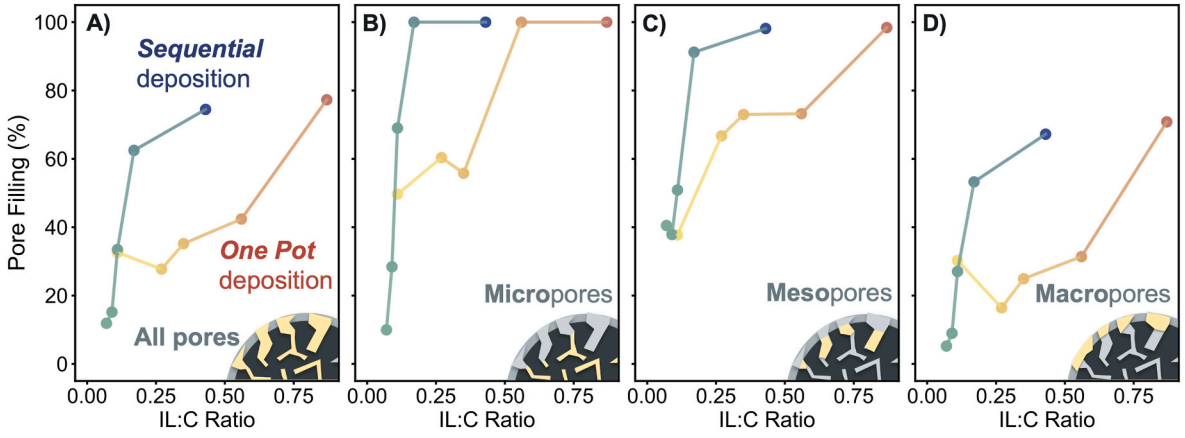

Fig. 2. Pore filling for A) total pores, B) micropores, C) mesopores, and D) macropores as a function of the nominal IL:C ratio.

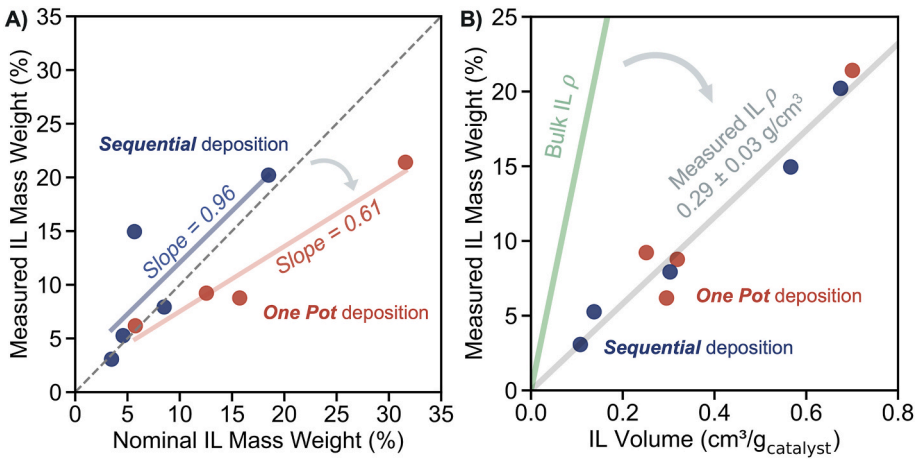

Fig. 3. A) Measured vs nominal IL mass weight. B) Measured IL mass weight as a function of the non-accessible BET volume. The bulk IL density of 1.5 g/cm^3 (from literature [30]) is represented by a green line, while the measured IL density was determined to be 0.29 ± 0.03 g/cm^3 (grey line). (For interpretation of the references to color in this figure legend, the reader is referred to the Web version of this article.)

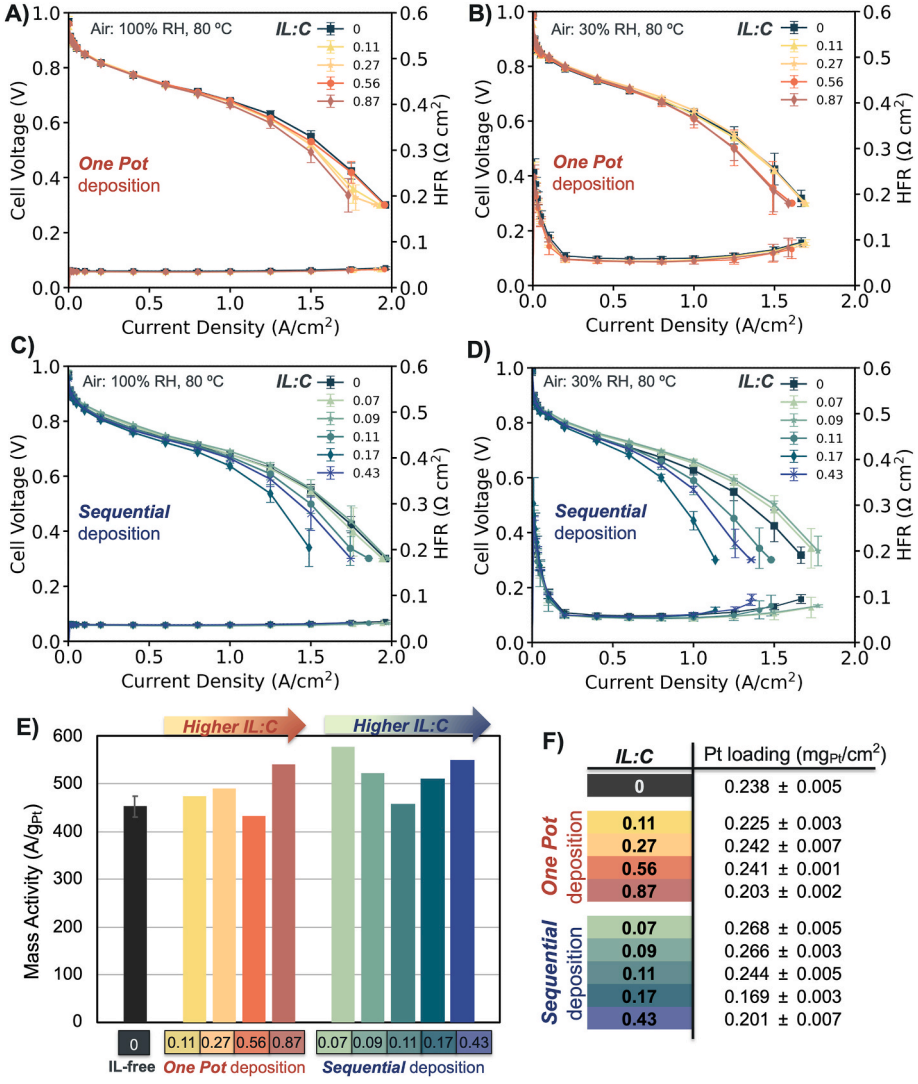

Fig. 4. Average H_2/Air performance data of fully conditioned 50 cm^2 MEAs at 150 kPa, 80 °C. A) One pot IL-samples at 100% RH B) One pot IL-samples at 30% RH C) Sequential deposition IL-samples at 100% RH D) Sequential deposition IL-samples at 100% RH. Error bars correspond to the standard deviation of 3 different tested MEAs. E) Mass activity ($i_m^{0.9V}$) of fully conditioned MEAs from H_2/O_2 performance at 150 kPa, 80 °C and 100% RH (cathodic sweep). F) Table with Pt loadings for the different synthesis methods and nominal IL:C ratios.

quickly achieves peak beginning of life (BOL) performance. It is possible that the IL and ionomer are restructuring during these steps, but it wasn't possible to quantify the change to pore filling or mass loading following electrode fabrication. Here, all fuel cell performance measurements and electrochemical characterizations have been performed on fully conditioned MEAs after the third voltage recovery cycle. Fig. 4 A), B), C), and D) show PEMFC performance during H_2/Air polarization curves measured at 80 °C, 150 kPa at wet (100% RH) and dry (30% RH) conditions, comparing the one-pot and sequential deposition electrodes against IL-free Pt/HSC MEA. IL-modified samples are labeled according to their IL:C ratios, maintaining consistency with the labeling used in previous plots, with the IL-free sample labeled as 0 IL:C. The IL-free Pt/HSC MEA shows consistent fuel cell performance comparable to previous benchmark Pt/HSC MEAs.

With water-saturated gas feeds, all IL-modified electrodes perform similarly or worse than the IL-free Pt/HSC electrode at 80 °C, 100% RH, 150 kPa_{abs}. Although there may be a slight enhancement at low current densities, the use of the IL adversely impacts performance at higher current densities for both the one-pot and sequential methods, especially at high IL loadings. The presence of IL within the cathode catalyst layer may impact ionic or gas transport. At lower RHs, sequential deposition samples with IL:C ratios of 0.07 and 0.09 (less than 40% micro and meso pore filling) show enhanced performance, particularly at higher current densities. IL-modified samples prepared via sequential deposition exhibit greater penetration of IL into the pores and overall higher synthesis efficiency based on BET and TGA experiments. The wider performance variability across sequential deposition samples is hypothesized to result from deposition deeper into smaller pores, potentially contacting more Pt sites. In contrast, the performance of one-pot deposition electrodes is less sensitive to nominal IL:C due to the limited effectiveness of IL deposition with this method.

While at higher current densities in wet conditions most IL-modified electrodes do not show any performance enhancement and suffer from mass transport limitations, these electrodes all have increased performance in the kinetic region. Fig. 4E shows cathodic mass activities at 0.9V (HFR-free) from H_2/O_2 performance at 150 kPa, 80 °C, and 100% RH. Overall, the IL-samples show 5–28% improved mass activity, which corresponds to ~1–7.5 mV improvement in performance. This aligns with the boost previously reported in a study of ILs in scale-up MEAs, where a maximum mass activity enhancement of ~20% was shown [27]. This improvement is less than the ~80–150 % reported for IL-modified catalysts in RDE systems, but still significant [20–26]. Only the OP 0.56 IL:C and SD 0.11 IL:C (80% and 55% micro and meso pore filling, respectively) exhibit slightly worse kinetic activity compared to the IL-free Pt/HSC electrodes. It is also worth noting that OP 0.56 IL:C had unexpectedly high IL loading based on *ex situ* quantification measurements, which may explain why it seems like an outlier across the OP series.

Fig. 4E also shows that one-pot deposition electrodes tend to increase ORR performance with increasing nominal IL:C ratio. This is expected since the one-pot deposition requires significant amounts of IL to fill all the micropores as shown in Figs. 1 and 2. For this reason, the OP samples do not reach a maximum mass activity until a relatively high IL:C ratio. However, the high IL:C ratio OP samples (OP 0.87 with 100% micro and meso pore filling) that exhibit the best kinetic activity are severely limited at lower RH and high current densities due to mass transport limitations. Conversely, the highest mass activity is observed on the SD electrode with the least amount of IL (SD 0.07). This electrode also shows enhancements in H_2/Air polarization curves at high current densities at 30% RH. The other samples (SD 0.09, 0.17, and 0.43) show slightly lower mass activity, but these values might not be statistically significant as they lie within the upper range of Pt/HSC activities (~500A/g_{Pt}). Because of the increased synthesis efficiency, we hypothesize that all SD can get to a significant MA enhancement even at very low IL loadings due to preferential filling of micropores. Therefore, SD samples with between 50 and 100% micropore filling exhibit the best performance at higher current densities because they don't suffer from mass transport due to excess IL within meso- and macropores, and adequate IL is present to promote kinetic activity.

To further evaluate the effect of ILs on both kinetic and high current density performance, electrochemical active surface area measurements (ECSA) were conducted via CO stripping experiments to assess whether the IL promotes Pt site accessibilities at different RHs. CO stripping measurements are preferred over H_{upd} from cyclic voltammetry experiments because the CO stripping peak area doesn't change as strongly with catalyst modifications (e.g. alloying) and can be measured at elevated temperatures. For the IL-free Pt/HSC sample, the ECSA decreases almost linearly as RH is lowered. This behavior is expected due to a combination of factors, including reduced ionomer conductivity and limited proton availability at lower RH, which restricts the accessibility of active Pt sites within micro- and mesopores. For IL-modified samples, one might anticipate that the incorporation of ionic liquids could mitigate these ECSA losses at reduced RH since ILs have intrinsic ionic conductivity. Improved connectivity could facilitate proton transport and preserve active site accessibility. However, as shown in Fig. 5, ECSA doesn't seem to have a trend as a function of IL:C ratio. Although the IL is expected to be beneficial, especially at lower RH, as demonstrated by the performance data, it appears that the ECSA matches the IL-free electrodes at those conditions. In contrast, at higher RH values, above 60% RH, we begin to see slight improvements, especially on SD electrodes.

Comparing the one-pot and sequential deposition methods, the SD approach yields less variant ECSA results, with a slight increase at higher RH. For the one-pot deposition, the ECSA shows greater variability across measurements. IL mobility at the interface could occur during different experiments and reaction conditions change as these additives are more mobile than the ionomer. Similarly, the variability of IL distribution in OP electrodes leads to the wider observed range of performance and ESCA. The less efficient OP deposition process may also lead to more IL being deposited in a disorganized manner. This may result in the IL being closer to the support surface rather than within the pores, leading to mobility of the IL and contributing to the observed variability in data across samples.

A previously established electrochemical impedance spectroscopy (EIS) technique was utilized to study the interactions of the ionomer at the HSC interface [17]. Using EIS, it is possible to measure double-layer capacitance (C_{dl}) and effective catalyst layer ionic resistance ($R_{cl,\ eff}$) as a function of operating conditions to elucidate how these electrode properties relate to the electrode utilization and H^+ conductivity at different conditions. Fig. S13 shows a characteristic Nyquist plot on Pt/HSC electrode measured in H_2/N_2, where the impedance data can be fit to a transmission line equivalent circuit model to extract double layer capacitance, effective H^+ transport resistance, and high frequency (ohmic resistance).

Fig. 6 and S14 show C_{dl} and $R_{cl,\ eff}$, normalized by the Pt loading, as a function of RH for the one-pot deposition and the sequential deposition IL-modified samples, respectively. For the IL-free Pt/HSC sample, the reduction in double-layer capacitance at lower RH reflects diminished electrochemical interface, as insufficient hydration disrupts the formation and stability of the electrochemical double layer, showing similar trends to ECSA. At low RH, we also see an increase in effective transport resistance, which arises from restricted proton transport within the ionomer and catalyst layers. Site-specific O_2 transport resistances are known to increase at low RH due to densification of ionomer thin films on catalytic sites. All these factors can contribute to heightened mass transport limitations and a decline in overall performance for HSC supports under these conditions.

The one-pot deposition IL-modified samples show a significant increase in C_{dl}, beginning with the sample plotted in the middle, which has a nominal IL:C ratio of 0.35. Since the one-pot samples have a relatively higher IL:C ratio, greater differences across the samples are expected due to the increased distribution of IL at the interface. In contrast, the sequential deposition samples (Fig. S14) generally follow the same trend

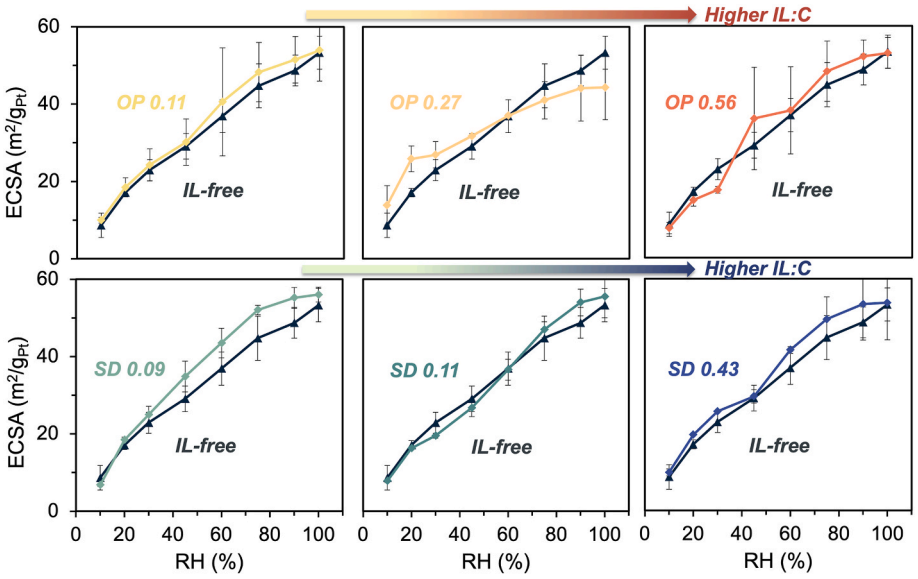

Fig. 5. Electrochemical active surface area (m^2/g_{Pt}) of fully conditioned MEAs determined by CO stripping as a function of RH.

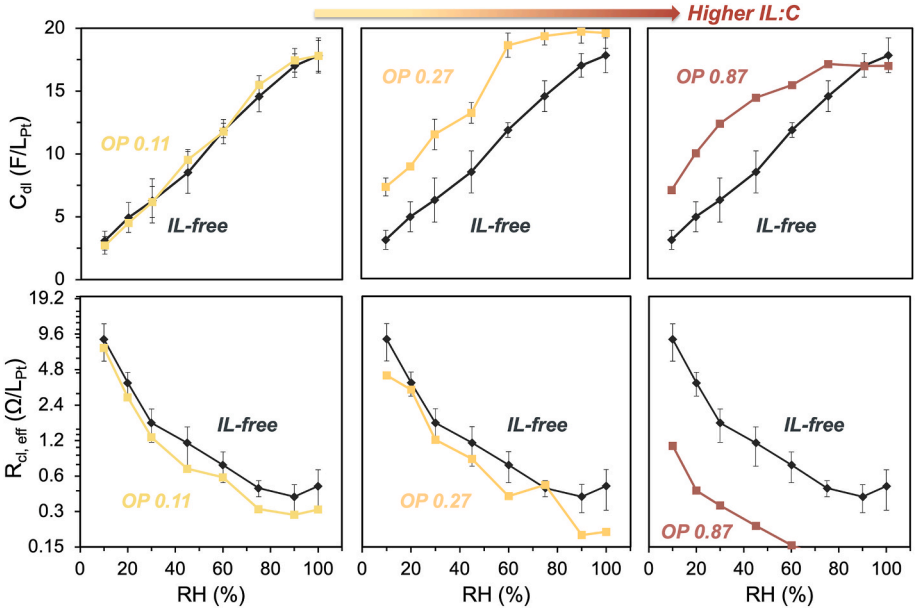

Fig. 6. Double-layer capacitance and catalyst layer ionic resistance as a function of RH for three one-pot deposition IL-modified samples.

and align with the IL-free samples. The same applies to the $R_{cl,\ eff}$ where we see a significant drop at high IL:C ratios and low RH for the one pot but similar trends for the sequential. At a specific IL loading, we might significantly improve the ionomer network by filling some of the disruption gaps that occur in a regular ionomer system. The ionic liquids may help bridge these gaps, creating a more robust network and enhancing both C_{dl} and $R_{cl,\ eff.}$ The enhancement of the ionomer network may not be as significant in the sequential deposition samples, as less IL is deposited on the surface due to its preferential filling of the micro- and mesopores. In the one-pot method, we hypothesize that more IL deposits on the surface or within the bulk electrode volume, which may increase mass transport limitations and hinder performance enhancements within catalyst particles. However, one-pot samples still show some interface improvements at higher IL:C ratios, where there is significant excess IL to penetrate the porous carbon as shown in the C_{dl} and $R_{cl,\ eff}$ plots.

While minimal differences in C_{dl} vs RH spectra suggest that the electrodes have very similar structures, we also investigated CO displacement to monitor sulfonate adsorption on the Pt surface. We hypothesize that, in the ionomer-ionic liquid system, not only can we observe an enhancement of kinetic performance due to improved transport properties, but also that the ionomer may improve network connectivity and increase the protection of active sites from sulfonate groups, consistent with prior fundamental RDE studies using ILs and ionomers [23].

Sulfonate adsorption was measured by CO displacement as a function of RH. Fig. 7 shows sulfonate coverage as a function of RH for both one-pot and sequential deposition IL-modified samples. As mentioned earlier, sequential deposition samples show less IL deposited on the exterior or macropore surfaces due to its preferential filling of the micro and mesopores. Consequently, this method may protect more Pt sites due to deeper IL penetration in the pores, having a higher IL percentage adsorbed on Pt sites. This is evident from Fig. 7, where even the sequential deposition samples with low IL:C ratios achieve very low

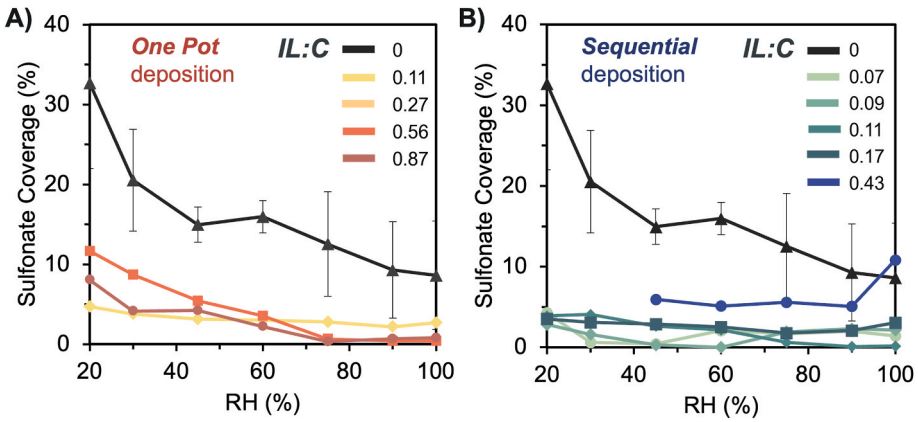

Fig. 7. Sulfonate coverage measured by CO displacement at 0.3 V_{cell} for IL-modified samples.

sulfonate coverage. When comparing a mid-range sequential deposition sample (0.11 IL:C ratio–55% micro- and mesopore filling) to the lowest one-pot sample with the same IL:C ratio, the results appear similar. However, at higher IL:C ratios (>80% micro and meso pore filling)–0.56 for the one-pot sample and 0.43 for the sequential sample—the sulfonate coverage approaches ~10%. This suggests the presence of IL within these samples prevents the direct interaction between ionomer and Pt sites, however, the extent of this effect depends greatly on IL:C ratio and IL distribution. The low sulfonate coverages on IL-modified electrodes suggest that the presence of IL on Pt sites after initial conditioning and testing, but further testing is required to quantify IL retention following durability testing.

The integration of ILs demonstrates the complex interplay between kinetic enhancements and mass transport limitations, resulting in a non-monotonic trend in performance as a function of nominal IL:C ratio, as plotted in Fig. 8. Note that the actual IL loading measured by TGA or BET may be a more accurate activity descriptor regardless of the synthesis method. At low IL loadings, insufficient pore filling (less than 30% total pore filling) limits the formation of a conductive ionomer-IL network, leading to suboptimal kinetic performance. Conversely, at high IL loadings (>60% total pore filling), while low-current-density kinetics benefit, excessive pore filling exacerbates mass transport resistances, especially when mesopores become increasingly filled. Sequential deposition consistently achieves more effective IL penetration into micropores at lower IL:C ratios compared to the one-pot method, resulting in superior control over pore filling and improved performance at intermediate IL:C ratios. This trend is reflected in H_2/air polarization curves under low RH conditions, where moderate IL loadings balance the trade-off between kinetic, ionic, and gas transport limitations. Supporting information further highlights the generality of these trends across higher potentials and operation at 90 °C (Fig. S17), where non-linear relationships persist, and IL-modified catalyst layers exhibit increased current densities. At 0.9 V, all IL-modified configurations achieve higher current densities compared to the IL-free baseline, paralleling the mass activity trends observed.

To assess the potential of pore filling data (Table S3) to predict electrode performance (Table S4) of IL-modified electrodes, linear regression analysis was performed using micropore, mesopore, macropore, and total pore filling to predict mass activity and current densities at 0.6 V, 0.7 V, 0.8 V, and 0.9 V measured at relevant heavy-duty polarization conditions (H_2/Air 90 °C, 40% RH, 250 kPa). Fig. S18 summarizes coefficients of determination (r^2) from the linear regression analysis for 24 pairwise correlations across SD, OP, and all samples (details in Supplemental Information). This analysis found weak correlations between pore filling and most fuel cell performance metrics, making it difficult to quantitatively predict fuel performance based solely on pore filling. The strongest observed relationship was the adverse effect of excess IL content (increased pore filling) on higher current density performance (current density at 0.6V) shown in Fig. S19 ($r \approx -0.83$). It's worth noting the lack of strong correlations may result from non-linear relationships between pore filling and performance metrics or changes in IL pore filling caused during electrode fabrication or testing.

3. Conclusions

Previous studies have provided valuable insights into IL chain length and IL:C ratios for MEA performance; however, few have delineated the

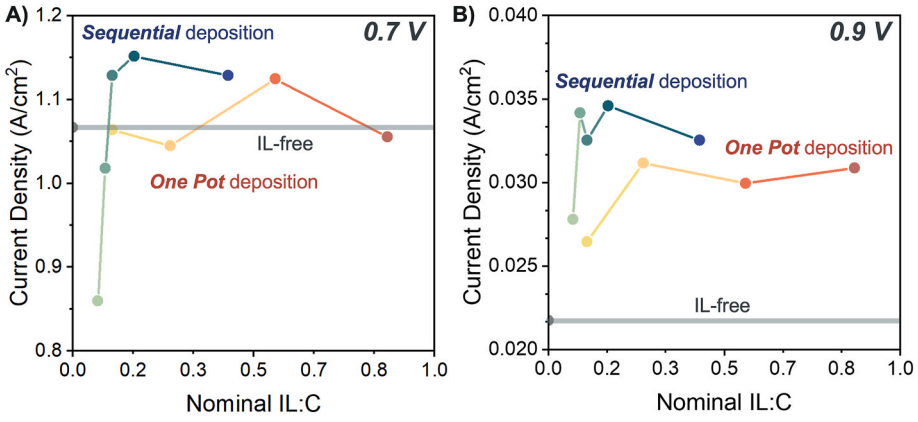

Fig. 8. Volcano plot of the current density at A) 0.7 V and B) 0.9V over nominal IL:C ratio. Performance data extracted from the H_2/Air: 40% RH, 90 °C, 0.7 V and 0.9 V polarization curves.

relationship between the effectiveness of the deposition method, IL pore penetration within the carbon support, and the subsequent influence on electrochemical properties. Bridging this knowledge gap establishes a framework for integrating ILs, and other catalyst additives, and establishes structure-performance relationships related to pore filling regimes. Through *ex situ* characterization of IL-modified Pt/HSC, this study found that the sequential deposition method was more efficient at penetrating carbon pores, resulting in higher IL loadings compared to a similar one-pot approach. At sufficient IL loadings, both methods showed small kinetic performance enhancements at 80 °C, 100% RH, while balancing improvements in $R_{cl,eff}$ against potential trade-offs in gas transport. We also see relevant enhancements in the mass transport at the high current density regions under low RH conditions. Observed mass activity enhancements cannot be fully attributed to changes in ECSA. Instead, these enhancements arise from a combination of improved ionic conductivity and reduced coverage of strongly adsorbed sulfonate species ($R–SO_4^-$) and protecting the active sites, underscoring the complex interplay between IL-mediated modifications to the catalyst microenvironment and overall performance. Moreover, this study emphasizes the importance of determining appropriate IL:C ratios to achieve desirable pore filling. Excessive IL loadings can lead to performance trade-offs and increased costs, as IL content exceeds what is necessary for effective micropore and mesopore filling. By selectively filling micropores and reducing overall IL usage through sequential deposition, our approach demonstrates that lower IL:C ratios can achieve improved performance at beginning of life without significantly impacting mass transport. Further testing of electrode durability to ensure IL retention throughout its lifetime is essential to assess the potential of IL additives within fuel cells. Future directions include the use of key design parameters to guide the incorporation of other ILs or similar additives with novel catalyst supports and electrode architectures, and enabling further improvements in performance and durability across diverse PEMFC applications.

4. Experimental methods

Synthesis of Ionic Liquids (IL). To synthesize 1-methyl-2,3,4,6,7,8-hexahydro-1H-pyrimido[1,2-a]pyrimidin-9-ium bis(perfluoroethylsulfonyl)imide ([MTBD][beti]), two approaches were used to assess differences in ionomer-ionic liquid network connectivity and IL penetration (impregnation) into pores. The IL precursors used were purchased at high purity and were not further refined before synthesis. MTBD, 7-methyl-1,5,7 triazabicyclo[4.4.0]dec-5-ene, Sigma Aldrich, 98% by specification, and 99.4%–100% by GC on the associated COA of different batches; lithium bis(perfluoroethylsulfonyl)imide, IoLiTec, was certified at >99% purity by NMR and ion chromatography, with both the lithium and bis(perfluoroethylsulfonyl)imide components individually reported at >99% and a measured water content below 1000 ppm.

The small residual fraction (<2%) is typically composed of trace water or low-level organic impurities (e.g., unreacted starting materials or solvent), but their exact identity is not reported by the suppliers. Given the low impurity levels and the fact that both synthesis routes (one-pot and sequential deposition) use the same commercially supplied reagents, we do not expect these trace impurities to affect the comparative trends or conclusions.

One pot deposition. First, the precursor [MTBD] (7-methyl-1,5,7-triazabicyclo[4.4.0]dec-5-ene, Sigma Aldrich, 98%) (2.51 g, 0.0164 mol) in water (100 mL) was cooled in ice to near 0 °C. 10 M HNO_3 solution (VWR, ACS, 70%) (1.47 g, 0.0164 mol) was added dropwise to the [MTBD] solution until a near neutral pH was reached. This was followed by the addition of lithium bis(perfluoroethylsulfonyl)imide (IoLiTec, 99%) (6.34 g, 0.0164 mol) into the 0.16M H[MTBD] solution. The mixture was then stirred for 1 h, and the IL was separated from the mixture as a viscous fluid phase beneath the aqueous phase. The resulting IL was washed 4 times with ultrapure water and dried overnight in a vacuum oven at 50 °C to obtain a colorless liquid.

To impregnate the catalyst with the prepared IL, first, the desired [MTBD][beti] mass was dispersed in IPA to get a 5 mg of IL/mL IPA solution. Then, the desired mass of TKK10E50E 50 wt% Pt/HSC was wetted in water to achieve 19 mg of catalyst/mL of water. The IL and catalyst dispersions were mixed together and ultrasonicated for 20 min to ensure uniform mixing. Finally, the sonicated dispersion was then transferred to a bigger vial with a magnetic stir bar and placed in an oil bath on a magnetic hotplate stirrer set at 50 °C. The solvents were slowly evaporated into the ambient atmosphere while continuously mixed with the magnetic stir bar. The obtained powder was further dried under vacuum at room temperature overnight.

Sequential deposition.[38,39] First, a 0.16 M H[MTBD] solution was prepared the same way as for the one-pot deposition. Then, the desired mass of TKK TEC10E50E 50 wt% Pt/HSC was wetted in water to achieve 5 mg of catalyst/mL of water. The desired volume of the 0.16 M H[MTBD] stock solution to achieve a desired mass of IL was then added to the wetted catalyst solution. The resulting solution was ultrasonicated for 60 min, followed by slow evaporation with the drying step in a vacuum oven at the end, a similar process as mentioned for the one-pot synthesis.

The catalyst impregnated with [MTBD] was then wetted to achieve 5 mg of catalyst/mL of water, and a desired mass of lithium bis(perfluoroethylsulfonyl)imide (IoLiTec, 99%) was then added to achieve the same moles in solution as the $[MTBD]^+$. The same ultrasonication, slow evaporation, and drying steps were used to obtain the final powder impregnated with [MTBD][beti].

Both approaches require the reaction to form the final form of the ionic liquid [MTBD][beti]. During the neutralization reaction of the [MTBD] precursor, a base, and nitric acid, the protonated base H $[MTBD]^+$ and nitrate anion NO_3^- are formed:

$$[MTBD] + HNO_3 \rightarrow [MTBD]^+ + NO_3^-$$

Then, an ion exchange occurs when Li[beti]) is added. Here, the $[beti]^-$ anion from Li[beti] pairs with protonated $[MTBD]^+$ to form the desired ionic liquid ([MTBD][beti]). The lithium cation (Li^+) pairs with the nitrate anion (NO_3^-) generated in the first step to form $LiNO_3$ as the byproduct:

$$[MTBD]^+ + Li[beti] \rightarrow [MTBD][beti] + LiNO_3$$

Any residual unreacted reagents are assumed to be washed out during the ink preparation, electrode fabrication, or initial electrochemical testing due to their solubility in solvents like IPA or water.

N_2 physisorption. Nitrogen gas physisorption was conducted with a Micromeritics 3Flex Adsorption Analyzer to study the porosity of the Pt/HSC and IL-modified Pt/HSC samples. The samples were first pretreated *ex situ* at 200 °C for 8 h under N_2 atmosphere using a Micrometrics Smartprep station. They were again preheated in situ and overnight to remove residual moisture after setting up the adsorption analyzer. Nitrogen physisorption was then performed at 77 K using ultra-high purity N_2 gas between a relative pressure (P/P_0) of 0 and 0.995. The protocol for determining the surface area and pore volume was adapted from Steinbach et al. [33] The specific total surface area was estimated by Brunauer–Emmett–Teller (BET) model. Pore volumes/areas and pore size distributions for mesopores (2–8 nm) and macropores (>8 nm) were determined by Barrett-Joyner-Halenda (BJH) model by using the desorption isotherms. T-plot model was used to estimate the micropore (<2 nm) volume/area [34].

Thermogravimetric Analysis. Thermogravimetric analysis (TGA) measurements were carried out in a platinum high-temperature treated pan (TA Instruments) with 20 mg mass sample using a Discovery TGA 55 (TA Instruments-Waters, LLC) controlled by Trios software. Firstly, these measurements were performed under N_2 atmosphere (flow of 10 mL/min) from 20 to 175 °C at 20 °C/min and stay isothermal for 30 min to pretreat the sample, eliminating mass loss due to adsorbed water. After

dehumidification, all weight loss in Pt/HSC samples is due to carbon oxidation and is not related to water desorption. The sample then underwent a stepwise isothermal treatment under air with a balance flow rate of 10 mL/min. The process began with an isothermal hold at the starting temperature for 15 min to stabilize the system. The temperature was then ramped at a rate of 20 °C/min to a target of 1000 °C. If the weight loss rate exceeded 1.000 wt%/min during the ramp, the temperature was held until the rate stabilized below 0.050 wt%/min before resuming. Upon reaching 1000 °C, the system was held isothermally until the weight loss rate dropped below 0.050 wt%/min.

Electrode Fabrication and Assembly. All catalyst-coated membranes (CCM) were prepared according to the established protocol [35,36]. Specifically, bare or IL-coated 50 wt% Pt/HSC (TKK, TEC10E50E) was dispersed into a mixture of ionomer (Nafion Dupont D2020), deionized water (DI), and n-propanol (n-PA) with the desired ionomer to carbon (I:C) mass ratio of 0.6. The catalyst suspensions were then dispersed with 20 s of horn sonication followed by 20 min of ice-bath sonication. The catalyst layer was ultrasonically sprayed onto NC700 membranes (supplied by Chemours) using a Sono-Tek spray station with a 25 kHz Accumist nozzle at target catalyst loadings for cathodes. Pt loadings on each individual electrode were verified by X-ray Fluorescence Spectroscopy (XRF) (Fisher XDV-SDD). Anode electrodes were prepared with Pt/HSC (TKK, TEC10E50E) dispersed in DI:n-PA (70 wt% water) with a I:C of 0.9 and a 0.1 mg_{Pt}/cm^2 loading.

Membrane Electrode Assembly - In situ Electrochemical Diagnostics. Once fabricated, the CCMs were assembled in a 50 cm^2 14 parallel channel (an) for fuel cell performance and double/triple (an/cath) serpentine flow field for electrochemical characterization. The CCMs were sandwiched between two 50 cm^2 Freudenberg (H23C8) gas diffusion layers (GDLs) at 18% compression. The CCMs, GDLs, and polytetrafluoroethylene (PTFE) gaskets were then placed between the flow fields, and the bolts tightened to 40 inch-pounds.

Break-in. The break-in procedures begin by heating the cell to 80 °C, and holding the cell at an open circuit potential (load equivalent flow rates of 0.8/2.5 = H_2/Air L_{std}/min), followed by a series of 5/10/5 voltage cycles in the fuel cell regime of 0.60 V–0.90 V for 4 min [32].

Voltage Recovery (VR). The voltage recovery (VR) step exposed the cell at 0.1 V under H2/Air (950/500 sccm, respectively) for 2 h at 40 °C and 150% RH [32].

H_2/O_2 Polarization Curves. The test protocol involved measuring the I-V curves from 0.7 V to OCV at 80 °C at 100 kPa O_2 partial pressure (150 kPa total pressure) and 100 % RH for 4 min per point (average of last 1 min used) in the anodic direction. The ORR mass activities were reported at 0.90 V after applying high-frequency resistance (HFR) and hydrogen crossover corrections.

H_2/Air Polarization Curves. The test protocol involved measuring the I-V curves from 0.3 V to OCV at 80 °C or 90 °C and at 150 kPa total pressure for 4 min per point (average of last 1 min used) in the anodic direction.

CO Stripping Voltammetry. Pt electrochemical surface area (ECSA) was determined by integrating the CO stripping charge (Q_{CO}) obtained from cyclic voltammetry (CV) after the introduction of CO to an equilibrated electrode held at 0.2 V_{cell}. The cathode feed was purged with pure N_2 at 0.25 L_{std}/min prior to the first anodic sweep. CVs were performed immediately at 80 °C and different RH under H_2/N_2 sweeping from 0.05 to 0.9 V at 20 mV/s 420 μC/cm^2 was assumed as the unit charge for CO integrated areas in determining the ECSA.

CO displacement Chronoamperometry. This method was used to measure the coverage of charged species on Pt/HSC at different cell potentials. At low potentials (0.1 V_{cell}), the negatively charged Pt surface adsorbs cationic species like H^+, which exhibit an oxidative current during CO displacement. By increasing the electrode potential, the electrode becomes more electron-deficient (initially less negatively charged, then more positively charged), leading to anion adsorption on the Pt surface. Experiments were conducted at 80 °C and 75% RH, while the electrode was held at 0.1, 0.2, 0.3, 0.4, and 0.5 V_{cell}. Ionomer coverages (Θ_{dis}) were determined by normalizing the displacement charges measured at 0.3 V by CO stripping charge (Q_{CO}).

Capacitance Coverage Experiments. EIS experiments were performed on fully conditioned 50 cm^2 MEAs using a Gamry Reference 3000 Potentiostat connected to a Gamry 30k Booster. EIS experiments were conducted at 80 °C with 1 atm pure H_2 and N_2 flowing at 100 cm^2/min at the anode and cathode gas lines, respectively. Experiments were run at 10, 20, 30, 45, 60, 75, 90, and 100% RH with 30–60 min equilibration time before each measurement. EIS was measured 50 kHz−50 mHz at 0.45 and 0.2 V versus RHE with ±10 mV oscillations for CO-free and CO-doped experiments, respectively. Cathodes were exposed to 1% CO/N_2 feed for 15 min to allow for CO adsorption, then purged with pure N_2 prior to CO-doped experiments. Residual CO was oxidized after CO-doped EIS experiments and before CO-free EIS measurements.

H_2/N_2 EIS fitting. The electrochemical impedance spectroscopy results were fitted to a transmission line equivalent circuit using the OSIF EIS fitting tool.[40] Due to electrode thickness, the spherical diffusion model gave better fits than the standard linear diffusion model.

CRediT authorship contribution statement

Marc Manyé Ibáñez: Writing – review & editing, Writing – original draft, Methodology, Investigation, Formal analysis, Conceptualization. **Adam Holewinski:** Writing – review & editing, Supervision, Resources, Funding acquisition. **J. Will Medlin:** Writing – review & editing, Supervision, Resources. **Tim Van Cleve:** Writing – review & editing, Writing – original draft, Visualization, Supervision, Resources, Project administration, Methodology, Formal analysis, Data curation, Conceptualization. **K.C. Neyerlin:** Writing – review & editing, Writing – original draft, Supervision, Resources, Project administration, Funding acquisition, Formal analysis, Conceptualization.

Declaration of competing interest

The authors declare that they have no known competing financial interests or personal relationships that could have appeared to influence the work reported in this paper.

Acknowledgements

This work was authored by the Alliance for Sustainable Energy, LLC, the manager and operator of the National Renewable Energy Laboratory for the U.S. Department of Energy (DOE) under Contract No. DE-AC36-08GO28308. Funding for materials, equipment, and staffing was provided by the U.S. Department of Energy Office of Energy Efficiency and Renewable Energy Hydrogen and Fuel Cell Technology Office as part of the Million Mile Fuel Cell Truck (M2FCT) Consortium, technology manager Greg Kleen. Funding for the graduate internship and manuscript writing was provided by the National Science Foundation (NSF) under award NSF CBET-1944834. The authors acknowledge the support of Doug Wymore, Cole Delery, and Ellis Klein related to the maintenance and capability improvements for the analytical and testing equipment utilized in this study. The views expressed in the article do not necessarily represent the views of the DOE or the U.S. Government. The U.S. Government retains and the publisher, by accepting the article for publication, acknowledges that the U.S. Government retains a nonexclusive, paid-up, irrevocable, worldwide license to publish or reproduce the published form of this work, or allow others to do so, for U.S. Government purposes.

Appendix A. Supplementary data

Supplementary data to this article can be found online at https://doi.org/10.1016/j.jpowsour.2026.239535.

Data availability

Data will be made available on request.

References

[1] S. Chu, Y. Cui, N. Liu, The path towards sustainable energy, Nature Mater 16 (1) (2017) 16–22, https://doi.org/10.1038/nmat4834.

[2] D.A. Cullen, K.C. Neyerlin, R.K. Ahluwalia, R. Mukundan, K.L. More, R.L. Borup, A. Z. Weber, D.J. Myers, A. Kusoglu, New roads and challenges for fuel cells in heavy-duty transportation, Nat. Energy 6 (5) (2021) 462–474, https://doi.org/10.1038/s41560-021-00775-z.

[3] Z.P. Cano, D. Banham, S. Ye, A. Hintennach, J. Lu, M. Fowler, Z. Chen, Batteries and fuel cells for emerging electric vehicle markets, Nat. Energy 3 (4) (2018) 279–289, https://doi.org/10.1038/s41560-018-0108-1.

[4] H.A. Gasteiger, N.M. Marković, Just a Dream—Or future reality? Science 324 (5923) (2009) 48–49, https://doi.org/10.1126/science.1172083.

[5] M.K. Debe, Electrocatalyst approaches and challenges for automotive fuel cells, Nature 486 (7401) (2012) 43–51, https://doi.org/10.1038/nature11115.

[6] E.H. Majlan, D. Rohendi, W.R.W. Daud, T. Husaini, M.A. Haque, Electrode for Proton exchange membrane fuel cells: a review, Renew. Sustain. Energy Rev. 89 (2018) 117–134, https://doi.org/10.1016/j.rser.2018.03.007.

[7] Borup, R.; Laboratory, L. A. N.; Weber, A.; Laboratory, L. B. N. M2FCT: Million Mile Fuel Cell Truck Consortium..

[8] X.X. Wang, M.T. Swihart, G. Wu, Achievements, challenges and perspectives on cathode catalysts in Proton exchange membrane fuel cells for transportation, Nat. Catal. 2 (7) (2019) 578–589, https://doi.org/10.1038/s41929-019-0304-9.

[9] X. Tian, X.F. Lu, B.Y. Xia, X.W. Lou, David, Advanced electrocatalysts for the oxygen reduction reaction in energy conversion technologies, Joule 4 (1) (2020) 45–68, https://doi.org/10.1016/j.joule.2019.12.014.

[10] T. Van Cleve, S. Khandavalli, A. Chowdhury, S. Medina, S. Pylypenko, M. Wang, K. L. More, N. Kariuki, D.J. Myers, A.Z. Weber, S.A. Mauger, M. Ulsh, K.C. Neyerlin, Dictating Pt-Based electrocatalyst performance in polymer electrolyte fuel cells, from formulation to application, ACS Appl. Mater. Interfaces 11 (50) (2019) 46953–46964, https://doi.org/10.1021/acsami.9b17614.

[11] T. Van Cleve, G. Wang, M. Mooney, C.F. Cetinbas, N. Kariuki, J. Park, A. Farghaly, D. Myers, K.C. Neyerlin, Tailoring electrode microstructure via ink content to enable improved rated power performance for platinum Cobalt/high surface area carbon based polymer electrolyte fuel cells, J. Power Sources 482 (2021) 228889, https://doi.org/10.1016/j.jpowsour.2020.228889.

[12] K. Kodama, A. Shinohara, N. Hasegawa, K. Shinozaki, R. Jinnouchi, T. Suzuki, T. Hatanaka, Y. Morimoto, Catalyst poisoning property of sulfonimide acid ionomer on Pt (111) surface, J. Electrochem. Soc. 161 (5) (2014) F649, https://doi.org/10.1149/2.051405jes.

[13] K. Shinozaki, Y. Morimoto, B.S. Pivovar, S.S. Kocha, Suppression of oxygen reduction reaction activity on Pt-Based electrocatalysts from ionomer incorporation, J. Power Sources 325 (2016) 745–751, https://doi.org/10.1016/j.jpowsour.2016.06.062.

[14] F.C. Cetinbas, R.K. Ahluwalia, N.N. Kariuki, V.D. Andrade, D.J. Myers, Effects of porous carbon morphology, agglomerate structure and relative humidity on local oxygen transport resistance, J. Electrochem. Soc. 167 (1) (2019) 013508, https://doi.org/10.1149/2.0082001JES.

[15] V. Yarlagadda, M.K. Carpenter, T.E. Moylan, R.S. Kukreja, R. Koestner, W. Gu, L. Thompson, A. Kongkanand, Boosting fuel cell performance with accessible carbon mesopores, ACS Energy Lett. 3 (3) (2018) 618–621, https://doi.org/10.1021/acsenergylett.8b00186.

[16] K. Shinozaki, H. Yamada, Y. Morimoto, Relative humidity dependence of Pt utilization in polymer electrolyte fuel cell electrodes: effects of electrode thickness, ionomer-to-carbon ratio, ionomer equivalent weight, and carbon support, J. Electrochem. Soc. 158 (5) (2011) B467, https://doi.org/10.1149/1.3556906.

[17] H. Iden, T. Mashio, A. Ohma, Gas transport inside and outside carbon supports of catalyst layers for PEM fuel cells, J. Electroanal. Chem. 708 (2013) 87–94, https://doi.org/10.1016/j.jelechem.2013.09.011.

[18] N. Ramaswamy, W. Gu, J.M. Ziegelbauer, S. Kumaraguru, Carbon support microstructure impact on high current density transport resistances in PEMFC cathode, J. Electrochem. Soc. 167 (6) (2020) 064515, https://doi.org/10.1149/1945-7111/ab819c.

[19] A. Avid, I.V. Zenyuk, Confinement effects for nano-electrocatalysts for oxygen reduction reaction, Curr. Opin. Electrochem. 25 (2021) 100634, https://doi.org/10.1016/j.coelec.2020.09.001.

[20] J. Snyder, T. Fujita, M.W. Chen, J. Erlebacher, Oxygen reduction in nanoporous metal–ionic liquid composite electrocatalysts, Nature Mater 9 (11) (2010) 904–907, https://doi.org/10.1038/nmat2878.

[21] Y. Li, T. Van Cleve, R. Sun, R. Gawas, G. Wang, M. Tang, Y.A. Elabd, J. Snyder, K. C. Neyerlin, Modifying the electrocatalyst–ionomer interface via sulfonated Poly (Ionic liquid) block copolymers to enable high-performance polymer electrolyte fuel cells, ACS Energy Lett. 5 (6) (2020) 1726–1731, https://doi.org/10.1021/acsenergylett.0c00532.

[22] G.-R. Zhang, T. Wolker, D.J.S. Sandbeck, M. Munoz, K.J.J. Mayrhofer, S. Cherevko, B.J.M. Etzold, Tuning the electrocatalytic performance of ionic liquid modified Pt catalysts for the oxygen reduction reaction via cationic chain engineering, ACS Catal. 8 (9) (2018) 8244–8254, https://doi.org/10.1021/acscatal.8b02018.

[23] G.-R. Zhang, M. Munoz, B.J.M. Etzold, Accelerating oxygen-reduction catalysts through preventing poisoning with non-reactive species by using hydrophobic ionic liquids, Angew. Chem. Int. Ed. 55 (6) (2016) 2257–2261, https://doi.org/10.1002/anie.201508338.

[24] Y. Li, S. Intikhab, A. Malkani, B. Xu, J. Snyder, Ionic liquid additives for the mitigation of nafion specific adsorption on platinum, ACS Catal. 10 (14) (2020) 7691–7698, https://doi.org/10.1021/acscatal.0c01243.

[25] R. Gawas, R. Sun, Y. Li, K.C. Neyerlin, Y.A. Elabd, M. Tang, J. Snyder, Characterization of a sulfonated Poly(Ionic liquid) block copolymer as an ionomer for Proton exchange membrane fuel cells using rotating disk electrode, J. Electrochem. Soc. 168 (12) (2021) 124511, https://doi.org/10.1149/1945-7111/ac4375.

[26] K. Huang, T. Song, O. Morales-Collazo, H. Jia, J.F. Brennecke, Enhancing Pt/C catalysts for the oxygen reduction reaction with protic ionic liquids: the effect of anion structure, J. Electrochem. Soc. 164 (13) (2017) F1448, https://doi.org/10.1149/2.1071713jes.

[27] A. Avid, J.L. Ochoa, Y. Huang, Y. Liu, P. Atanassov, I.V. Zenyuk, Revealing the role of ionic liquids in promoting fuel cell catalysts reactivity and durability, Nat. Commun. 13 (1) (2022) 6349, https://doi.org/10.1038/s41467-022-33895-5.

[28] H. Luo, G.A. Baker, J.S. Lee, R.M. Pagni, S. Dai, Ultrastable superbase-derived protic ionic liquids, J. Phys. Chem. B 113 (13) (2009) 4181–4183, https://doi.org/10.1021/jp901312d.

[29] S. Lowell, J.E. Shields, M.A. Thomas, M. Thommes, Characterization of Porous Solids and Powders: Surface Area, Pore Size and Density; Scarlett, B., Series Ed.; Particle Technology Series, Springer Netherlands, Dordrecht, 2004, https://doi.org/10.1007/978-1-4020-2303-3.

[30] L. Fan, Y. Wang, K. Jiao, Enhancing oxygen transport in the ionomer film on platinum catalyst using ionic liquid additives, Fundam. Res. 2 (2) (2022) 230–236, https://doi.org/10.1016/j.fmre.2021.09.004.

[31] O.A. Baturina, S.R. Aubuchon, K.J. Wynne, Thermal stability in air of Pt/C catalysts and PEM fuel cell catalyst layers, Chem. Mater. 18 (6) (2006) 1498–1504, https://doi.org/10.1021/cm052660e.

[32] J. Zhang, L. Paine, A. Nayar, R. Makharia, Methods and processes to recover voltage loss of pem fuel cell stack. US20110195324A1. https://patents.google.com/patent/US20110195324A1/en%0A, August 11, 2011. (Accessed 24 May 2025).

[33] F. Fait, J.C. Steinbach, A. Kandelbauer, H.A. Mayer, Impact of porosity and surface functionalization of hard templates on the preparation of mesoporous Silica microspheres, Microporous Mesoporous Mater. 351 (2023) 112482, https://doi.org/10.1016/j.micromeso.2023.112482.

[34] T. Soboleva, X. Zhao, K. Malek, Z. Xie, T. Navessin, S. Holdcroft, On the Micro-, Meso-, and macroporous structures of polymer electrolyte membrane fuel cell catalyst layers, ACS Appl. Mater. Interfaces 2 (2) (2010) 375–384, https://doi.org/10.1021/am900600y.

[35] M. Wang, J.H. Park, S. Kabir, K.C. Neyerlin, N.N. Kariuki, H. Lv, V.R. Stamenkovic, D.J. Myers, M. Ulsh, S.A. Mauger, Impact of catalyst ink dispersing methodology on fuel cell performance using In-Situ X-Ray scattering, ACS Appl. Energy Mater. 2 (9) (2019) 6417–6427, https://doi.org/10.1021/acsaem.9b01037.

[36] S. Kabir, D.J. Myers, N. Kariuki, J. Park, G. Wang, A. Baker, N. Macauley, R. Mukundan, K.L. More, K.C. Neyerlin, Elucidating the dynamic nature of fuel cell electrodes as a function of conditioning: an Ex situ material characterization and in situ electrochemical diagnostic study, ACS Appl. Mater. Interfaces 11 (48) (2019) 45016–45030, https://doi.org/10.1021/acsami.9b11365.